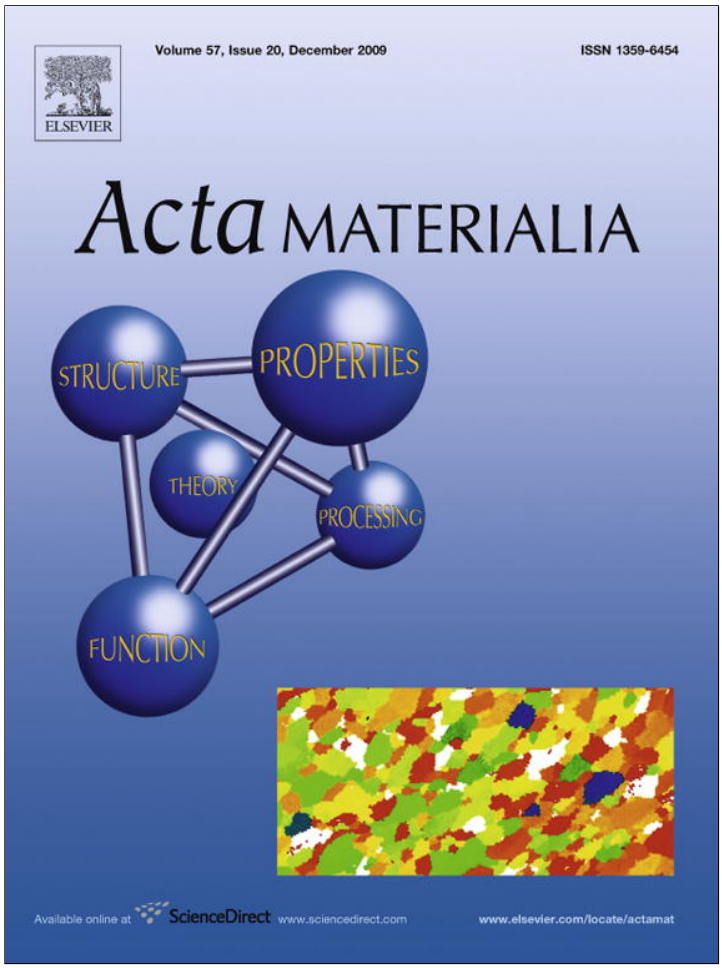

Available online at www.sciencedirect.com
ScienceDirect
Acta Materialia 57 (2009) 6013–6021
Acta MATERIALIA
www.elsevier.com/locate/actamat

Experiments and modeling of rapid solidification of plasma-sprayed yttria-stabilized zirconia

H. Liu [a], H.R. Salimi Jazi [a,b], M. Bussmann [a,*], J. Mostaghimi [a]

[a] Department of Mechanical and Industrial Engineering and Centre for Advanced Coating Technologies, University of Toronto, 5 King's College Road, Toronto, ON, Canada M5S 3G8
[b] Department of Materials Engineering, Isfahan University of Technology, Isfahan, Iran, 8415683111

Received 27 February 2009; received in revised form 28 June 2009; accepted 12 August 2009
Available online 11 September 2009

Abstract

Thermal barrier coatings (TBCs) are widely used to increase the working temperature and improve the high-temperature corrosion resistance of base materials. Thermal spraying methods such as air plasma spraying (APS) are convenient techniques to deposit TBCs. This work examines the rapid solidification of APS-deposited yttria-stabilized zirconia (YSZ), by modeling the non-equilibrium solidification of a single molten particle. The model solves the so-called hyperbolic equations for heat and mass transfer to predict interface undercooling and velocity as a function of time, and also predicts the morphology of the solidification front (and thus the microstructural characteristics of rapidly solidified YSZ) as a function of interface velocity. Results are presented of a single particle solidifying onto a steel substrate, and onto a previously deposited particle. The numerical results are also compared to experimental data of the microstructure of a YSZ splat deposited by APS, to validate the model.

Keywords: YSZ; Rapid solidification; Non-equilibrium; Undercooling; Capillarity

1. Introduction

Thermal barrier coatings (TBCs) are widely used to increase the working temperature, improve the high-temperature corrosion resistance, and protect the base materials of high-temperature turbine and engine parts for aircraft and diesel vehicles. The substrate materials in these applications are usually superalloys; the TBC consists of a thin bond coat that serves as an intermediate layer, and a relatively thick ceramic top coat. The ceramic heat-insulating layer can reduce the surface temperature of hot sections by as much as 100–200 °C [1].

In general, TBCs should have a low thermal conductivity, adequate adherence (which is a function of good interparticle bonding and a strong coating–substrate bond), a coefficient of thermal expansion (CTE) similar to that of the substrate, resistance to mechanical stresses that can result in cracking and loss of coating, adequate stabilization to inhibit structural transformation during engine operation, resistance to high-temperature oxidation of the coating and coating–substrate interface, and repairability during manufacturing and after service operations.

Among various types of ceramic TBC materials, zirconia ceramics (ZrO_2) possess some of these characteristics, and have excellent mechanical properties such as high fracture strength and toughness. They have a high CTE, similar to that of typical base materials, and low thermal conductivity. Unfortunately, zirconia coatings exhibit degradation of mechanical properties due to solid phase transformations at various temperatures. Zirconia has three stable crystal structures (allotropy) at atmospheric pressure depending on temperature: monoclinic below 1170 °C, tetragonal between 1170 and 2370 °C, and cubic above 2370 °C up to the melting point (2680 °C) [2]. Tetragonal zirconia exhibits high toughness and strength, but to avoid

* Corresponding author. Tel.: +1 416 978 1275; fax: +1 416 978 7753.
E-mail address: bussmann@mie.utoronto.ca (M. Bussmann).

1359-6454/$36.00 © 2009 Acta Materialia Inc. Published by Elsevier Ltd. All rights reserved.
doi:10.1016/j.actamat.2009.08.023

failure of a zirconia coating during thermal cycling the tetragonal phase must be stabilized to suppress the tetragonal-to-monoclinic transformation upon cooling below 1170 °C. Usually between 6 and 10 wt.% yttria (Y_2O_3) is used to stabilize zirconia. Yttria-stabilized zirconia (YSZ) coatings are widely used as TBCs for turbines and diesel engines because of their high-temperature phase stability, low thermal diffusivity, and high CTE [3,4].

Two methods are widely used to deposit TBCs: atmospheric plasma spraying (APS) and electron beam physical vapor deposition (EBPVD). The advantages of using APS to deposit YSZ include a high deposition rate that can easily yield thick coatings of a few millimeters, and the formation of porosity in these coatings. In APS, the coating material is injected as powder particles into a high-temperature, high-velocity environment generated by a DC arc plasma, that then melt and accelerate towards the substrate. Upon impact, the particles solidify rapidly at conditions that are far from equilibrium.

When the cubic phase of YSZ undergoes a diffusionless transformation to the tetragonal phase (see Fig. 1), any of the cubic phase axes can become the tetragonal axes, and so one would expect three variants in the equilibrium tetragonal phase. Liquid YSZ can also nucleate directly to the tetragonal phase due to undercooling, but then the only tetragonal variant axis one would expect would be along the direction of grain growth, due to the isotropy of crystallization. Chraska and King [5] used transmission electron microscopy to study the microstructure and phase of single YSZ splats sprayed on a smooth hot surface, and found columnar grains of a metastable tetragonal phase that lacked at least one of the variants, which indicates that the tetragonal phase was formed directly from the liquid phase.

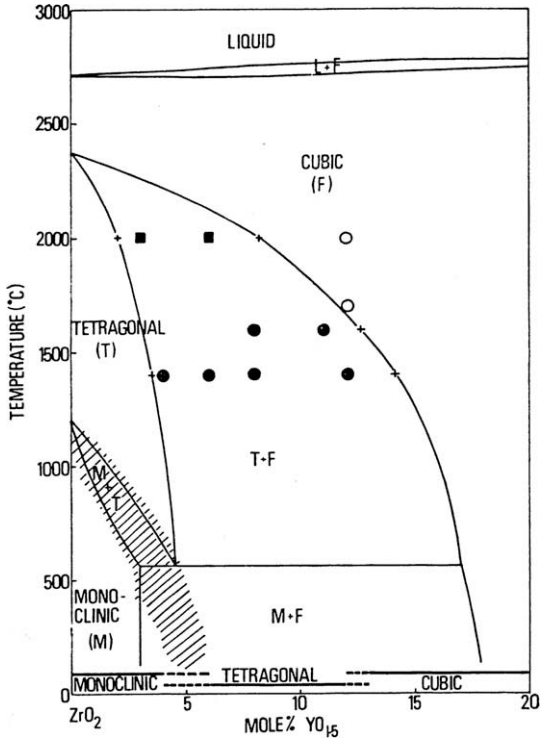

Fig. 1. Phase diagram for the zirconia-rich portion of the zirconia–yttria system [5].

Plasma-sprayed TBCs are an agglomeration of numerous splats of molten and partially molten particles that are connected by mechanical and metallurgical bonding. The boundaries between splats are associated with porosity and microcracks. Thus, the microstructure and properties of a TBC coating, as characterized by grain morphology, grain size, and microsegregation, are directly related to individual splat morphology and crystal structure, and the adhesion between the TBC and substrate as well as between individual splats. A variety of factors affect the solidification behavior of a splat: in-flight particle characteristics such as temperature and velocity, the substrate material and its surface properties (including temperature and roughness), and the thermal contact resistance caused by gases and solid impurities trapped at the splat–substrate interface [4,6–8]. For an overview of thermal spray splat formation, see the review by Chandra and Fauchais [9].

In recent years, several experimental studies (e.g. [6–8]) have examined the microstructure of an APS deposit, focusing on the final morphology of solidified splats and the associated solidification behavior, to gain a better understanding of the fundamental mechanisms of rapid solidification and microstructure formation during plasma spraying. In this study we examine YSZ single splat solidification, both experimentally and numerically, to visualize how rapid solidification influences grain formation in the microstructure. The grain structure of a single YSZ splat was studied experimentally using a focused-ion-beam (FIB) microscope. The numerical model was then used to simulate the rapid solidification of a splat, both on a substrate and on a previously deposited splat, to study grain formation and local non-equilibrium effects related to the solid–liquid interface velocity, and capillarity effects were also modeled, to predict grain size and to validate the numerical results. The model is built on that of Wang et al. (e.g. [10,11]). Finally, it should be noted that others too have developed models of rapid solidification of other thermal sprayed materials (e.g. [12,13]), that also attempt to link predictions of interface velocity and undercooling to microstructure.

2. Experiments

2.1. Experimental procedure

YSZ was sprayed with a SG-100 plasma torch (Praxair, Concord, NH, USA). The APS operating parameters and conditions are summarized in Table 1.

Single splats of agglomerated ZrO_2–8%Y_2O_3 powder (Metco 204B-NS, Sulzer Metco, USA), with particle diameter between 45 and 75 μm, were collected on stainless steel substrates (20 mm × 20 mm × 1.4 mm thick). The substrates were polished (the arithmetic average height of the roughness was 0.19 μm [4]) in order to obtain uniform splats that could more easily be analyzed. The substrates

Table 1
APS process parameters.

Gun	SG-100
Current (A)	630
Total gas flow rate (Ar/He) (slpm)	50/20
Powder carrier gas (Ar) (slpm)	9.5
Feed rate (g min^{-1})	8
Spray distance (mm)	50
Substrate temperature (°C)	300
Plasma gun thermal efficiency (%)	40–45

were maintained at a constant temperature of 300 °C by using a J-type thermocouple, an electrical heater, and a temperature controller. This is above the so-called "transition temperature" of YSZ [6], above which splat deposition is characterized by less splashing and so yields splats that are more disk-shaped than fragmented.

Fig. 2 illustrates the experimental setup. A shielding plate with a 2 mm hole in the center was used to obtain relatively uniform particle conditions, by isolating single particles traveling along the center of the plasma plume. The stainless steel substrate was positioned behind the shielding plate, for a total spraying distance of 50 mm. By sweeping the substrate through a stream of particles, individual splats were collected on the substrate. Particle conditions upon impact were monitored by a DPV-2000 system (Tecnar Ltd., Montreal, Canada). Particles at 50 mm from the plasma gun had a velocity of 125 ± 21 m s^{-1} and a temperature of 2592 ± 189 °C.

Individual splats were cross-sectioned by a FIB milling machine (Micrion Corporation, Peabody, MA, USA) equipped with a scanning electron microscope to image the cross-section. To explore the grain structure in the splats, the cross-sections were polished and etched by Ga ions using the FIB machine.

2.2. Experimental results

Micrographs in Fig. 3 show the top view and cross-section of a single YSZ splat deposited on a polished stainless steel substrate at 300 °C. Fig. 3a illustrates the final morphology of the splat after impact. The final diameter is approximately 180 μm. Splat curl up can be observed at the edges of the splat, and finger formation and splashed particles can be clearly seen. The cross-section AA of the same splat is illustrated in Fig. 3b. The very bottom of the splat is a thin layer of a very fine equiaxed grain microstructure (average grain size <100 nm), that formed when the molten droplet first impacted the substrate. Above this equiaxed layer, a columnar grain morphology (average grain size <100 nm) is visible.

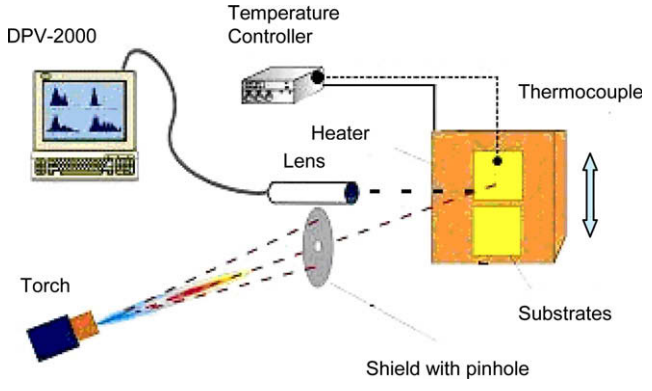

Fig. 2. Experimental setup for single splats collection.

We focus in this paper on the growth of the columnar grain morphology, which begins when the temperature of molten YSZ atop the equiaxed layer reaches the nucleation temperature. The nucleated grains grow laterally until the layer is completely covered, and then columnar grains begin to grow in the direction opposite the heat flux. At this stage, the temperature gradient is very high, and so the columnar solidification is partitionless, and the interface planar. The heat of fusion released during this initial solidification increases the temperature of liquid above the solidified layer, and so the subsequent growth rate is limited by the rate of heat transfer, suppressing nucleation and leading to columnar crystal growth. There is then competition between grains: the average column above the equiaxed structure (Fig. 3b) is around 100 nm wide. The final grain size depends on the nucleation density and on the lateral competition, and will be analyzed numerically [14].

3. Numerical simulation

3.1. Governing equations, boundary and initial conditions

During the rapid solidification of APS-deposited YSZ, the solidification front grows much more quickly than during an equilibrium solidification process [11]. Yet YSZ has a low diffusive speed $V_D \sim 1$ m s^{-1} [11]. As a result, use of the traditional Fourier's and Fick's laws is questionable, because they assume an infinite velocity of heat and mass propagation [15]. A more general approach is a hyperbolic model obtained by adding a relaxation term (proportional to a relaxation time τ_D) to the standard parabolic diffusion equations. τ_D may be thought of as the time interval necessary for atoms on the liquid side of an interface to jump onto the neighboring solid lattice, and can be defined as $\tau_D \equiv \frac{D}{V_D^2}$, where D is the mass diffusivity and V_D is the diffusive speed.

The addition of relaxation terms to Fourier's and Fick's laws results in more general diffusion equations. Combining these laws with equations for conservation of energy and concentration yields the following hyperbolic equations [15]:

$$\frac{\partial T_j}{\partial t} + \tau_D \frac{\partial^2 T_j}{\partial^2 t} = \alpha_j \nabla^2 T_j \tag{1}$$

$$\frac{\partial C_j}{\partial t} + \tau_D \frac{\partial^2 C_j}{\partial t^2} = D_j \nabla^2 C_j \tag{2}$$

$\alpha_j = \frac{\kappa_j}{\rho_j C_{p_j}}$ is the thermal diffusivity, the subscript j represents one of the phases, κ the thermal conductivity, ρ the density, and C_p is specific heat at constant pressure. Notice that

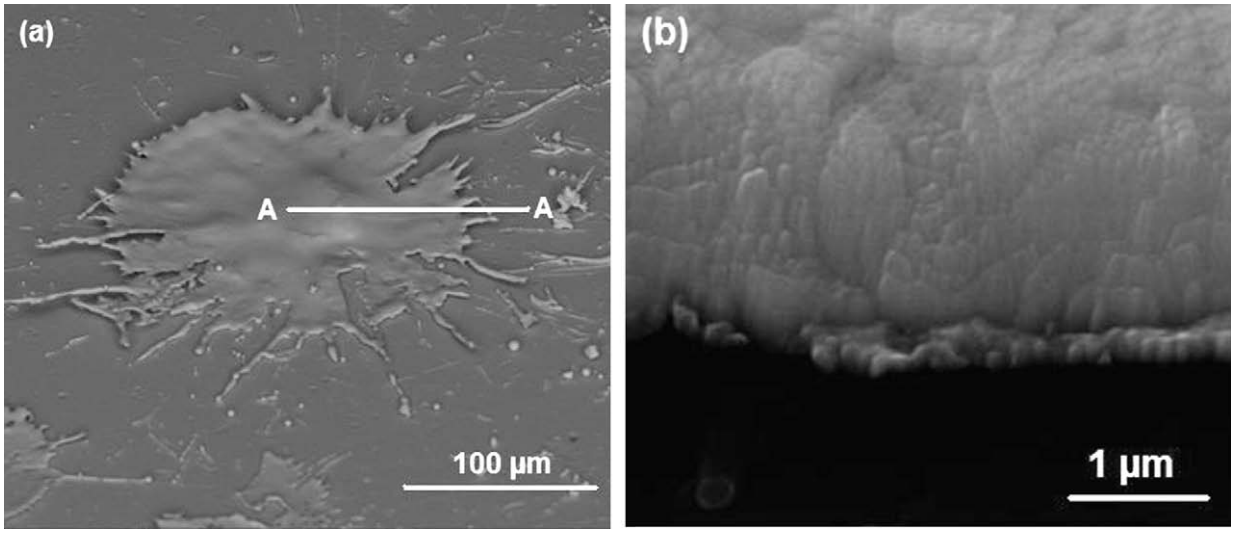

Fig. 3. Micrographs obtained from a FIB microscope: (a) top view of a single splat and (b) cross-section of a splat, showing both equiaxed and columnar grain microstructures.

when τ_D is zero, the above equations revert to the standard parabolic ones, which are appropriate for near-equilibrium solidification.

To analyze the extent of non-equilibrium behavior is to compare the magnitudes of the solid/liquid interface velocity V_i and the diffusive speed V_D of the melt. When V_i is comparable to but smaller than V_D, solute propagation is a joint process of diffusion and wave propagation [16]. As V_i approaches V_D, the wave mechanism dominates. When $V_i > V_D$, diffusion in the liquid ceases, and solidification is then diffusionless. Hence, the extent of non-equilibrium behavior is related to the relative magnitudes of V_i and V_D, and if these velocities are comparable, then concentration-induced non-equilibrium effects will be more pronounced.

Eqs. (1) and (2) are solved across a thin molten layer that suddenly contacts a substrate, subject to initial, boundary and dynamic interface conditions. The initial conditions are:

$$T(x,0) = T_o, \quad C(x,0) = C_0, \quad J(x,0) = J_C(x,0) = 0 \tag{3}$$

where T_0 and C_0 are the initial temperature and concentration, and J and J_C are temperature and concentration fluxes. At the upper surface of the splat ($x = b$):

$$J(b,t) = J_C(b,t) = 0 \tag{4}$$

At the base of the splat, we simplify the thermal boundary condition by introducing a heat transfer coefficient h and a substrate temperature T_∞, and assume no mass transfer:

$$J(0,t) = h[T(0,t) - T_\infty], \quad J_C(0,t) = 0 \tag{5}$$

The assumption that splat cooling occurs entirely through the substrate has been well-justified previously (e.g. [17]). Dynamic interface conditions include expressions of energy and concentration conservation, and an interface undercooling condition. The energy conservation equation is:

$$L \cdot C_P^{-1} \cdot V_i = J_L - J_S \tag{6}$$

where L is the latent heat, and J_L and J_S represent the heat fluxes from the liquid and solid sides of the solidification front. The corresponding conservation equation for concentration is:

$$(C_L - C_S) \cdot V_i = J_{C_L} \tag{7}$$

where C_L and C_S are the solute concentrations on the liquid and solid sides of the solidification front, related via the partition coefficient: $C_S = k_f C_L$. J_{C_L} is the concentration flux on the liquid side; we assume the flux on the solid side to be zero, since the mass diffusivity within the solid is orders of magnitude less than within the liquid.

The interface undercooling condition is an extra constraint on the governing equations [11]:

$$T_i = T_m + m \cdot C_L - V_i/\mu + \Gamma \cdot K \tag{8}$$

T_i is the interface temperature, T_m the equilibrium melting temperature, m the slope of the non-equilibrium liquidus, Γ the capillarity constant, K the mean curvature of the grain tip, and μ is the kinetic coefficient of interface motion.

What remains is to specify the partition coefficient k_f and the liquidus slope m as functions of the equilibrium values k_e and m_e; we used the expressions derived by Galenko and coworkers [18] that are functions of V_i/V_D:

$$k_f = \frac{k_e(1 - V_i^2/V_D^2) + V_i/V_D}{1 - V_i^2/V_D^2 + V_i/V_D}, \quad V_i < V_D \tag{9}$$

$$k_f = 1, \quad V_i \geq V_D \tag{10}$$

Note that the second expression indicates complete solute trapping when the interface velocity exceeds the diffusion velocity. Similarly,

$$m = \frac{m_e}{1 - k_e}[1 - k_f + \ln(k_f/k_e) + (1-k)^2(V_i/V_D)], \quad V_i < V_D \tag{11}$$

$$m = \frac{m_e \ln k_e}{k_e - 1}, \quad V_i \geq V_D \tag{12}$$

3.2. Predicting morphology and grain size

In addition to solving for the temperature and concentration fields and the interface velocity, we also wish to predict the morphology of the solidification front, which can be planar, dendritic, or cellular, and the grain size, the calculation of which depends on the morphology.

If the solid/liquid interface is initially planar, then the grain size is directly related to the nucleate size, because in this case there is no competition between grains. If, on the other hand, the solid/liquid interface is initially cellular, or transforms from planar to cellular, then neighboring grains compete as they grow, and the grain size must be calculated based on marginal stability theory.

To determine the grain size for a planar interface, nucleation theory is required, as the grain size is determined by a balance between the nuclei density and the nuclei growth rates at the onset of solidification. The theory can be simply explained: on the one hand, the average nucleation rate per unit area depends on the nucleation temperature and undercooling; on the other hand, the nuclei density depends on the nuclei growth velocity and the time required to cover the substrate surface. Combining these relations, the average grain size λ can be written as [5]:

$$\lambda^3 = \frac{8a\left[1 - \exp\left(-\frac{L\Delta T_r}{RT}\right)\right]}{\pi n \exp\left(-\frac{c}{\Delta T_r^2 R T_i}\right)} \tag{13}$$

where ΔT_r is the curvature-induced undercooling, a the interatomic spacing, R the universal gas constant, n is the nucleation site density, and c is a constant.

From Eq. (13), Chraska and King [5] obtained an average grain size as a function of melt undercooling for YSZ splats quenched on a steel substrate. As indicated in Fig. 4, the average grain size decreases as the nucleation temperature drops; for grain sizes less than 100 nm, the nucleation temperature is less than 2100 °C.

If the solid/liquid interface is initially cellular or transforms from planar to cellular, then the grain size must be determined via theories of microstructural transition. In what follows, we briefly present a length scale-based theory that identifies the dominant physical mechanism behind the transition that occurs during the rapid solidification of YSZ. We follow that with expressions for grain size obtained from stability theory.

Fig. 5 [19] illustrates the relationship between the solidification front morphology (planar, cellular and dendritic), the temperature gradient, and the interface velocity. When the temperature gradient is low, a sequence of microstructural transitions occurs as the interface velocity increases: planar to cellular to dendritic, then back to cellular, and finally planar. As the temperature gradient increases, the initial planar to cellular transformation occurs at increasingly higher interface velocities. Finally, there is a critical

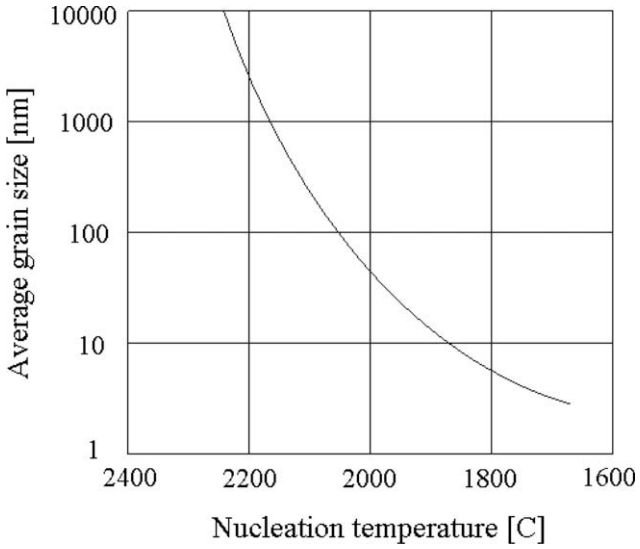

Fig. 4. Average grain size (width of columnar grains) as a function of the melt undercooling, for a YSZ splat quenched on a steel substrate [5].

velocity on the order of the diffusive speed beyond which the interface is planar regardless of temperature gradient that leads to solute trapping.

These transitions have been associated with various characteristic lengths [20]. Specifically, the planar to cellular transition at high interface velocity is driven by the interplay of solutal diffusion and capillarity effects, and the transition is said to occur when $l_D \sim k d_0$ ($l_D = D/V_i$ is a solutal diffusion length, $d_0 = \Gamma/\Delta T_s$ is a capillarity length, Γ is the Gibbs–Thompson coefficient, k is the partition coefficient, and $\Delta T_s = -m(C_L - C_S)$ is the constitutional undercooling). Based on this argument, the following is an order-of-magnitude expression for the cellular spacing λ [20]:

$$\frac{1}{\lambda^2} = \left(\frac{1}{l_D d_0}\right)\sigma^* - \left(\frac{1}{l_T d_0}\right)\sigma^* \tag{14}$$

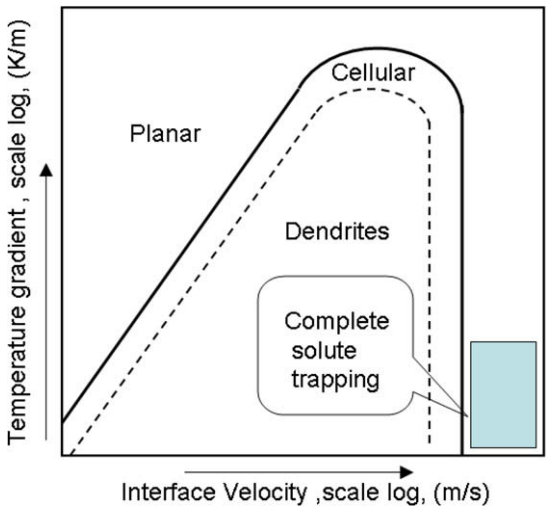

Fig. 5. Interface morphology (planar, cellular dendritic) transformations [19].

where σ^* is a constant and l_T a thermal length. Eq. (14) relates grain size to $m\xi_C G_C - G$ (ξ_C a concentration stability parameter; G and G_C represent the temperature and concentration gradients on the liquid side of the interface) and to the effect of capillarity, proportional to Γ.

A more precise expression for the grain tip radius $R(\sim \lambda)$ can be determined from marginal stability analysis [21], by relating the stability limit of the capillarity effect to the shortest wavelength of a perturbation:

$$R = \Gamma^{0.5}\left[4\pi^2 m\xi_C G_C \frac{(\Psi-1)}{\Psi}\right]^{-0.5}, \quad V_i < V_D \tag{15}$$

where

$$\Psi = \frac{m\xi_C G_C}{\frac{\kappa_L}{\kappa_L+\kappa_S}\xi_L G_L + \frac{\kappa_S}{\kappa_L+\kappa_S}\xi_S G_S} \tag{16}$$

Note that Ψ is the ratio of a concentration gradient term ($m\xi_C G_C$) to a temperature gradient $\left(\frac{\kappa_L}{\kappa_L+\kappa_S}\xi_L G_L + \frac{\kappa_S}{\kappa_L+\kappa_S}\xi_S G_S\right)$ term; the three ξ are stability parameters defined by Trivedi and Kurz [21]. Similar to Eq. (14), Eq. (15) also relates the cellular to planar transformation to Γ, G and G_C.

Returning to APS-deposited YSZ, when a molten particle impacts a substrate, the liquid cools beneath the equilibrium melting temperature, while the solute remains uniformly distributed, and so $\Psi \ll 1$ because the temperature gradient is much larger than the corresponding concentration gradient. Eq. (16) then yields no real solution, which implies that the initial solidified interface is planar. Once solidification begins, solute quickly accumulates on the liquid side of the interface and the local concentration gradient increases; at the same time the temperature gradient decreases as latent heat release compensates for the heat loss to the substrate; the combination of these two trends drives $\Psi \to 1$. The planar to cellular transformation occurs when $\Psi = 1$, when Eq. (16) begins to yield a pair of real solutions for the grain size, that correspond to the upper and lower limits of the size range.

4. Numerical results and discussion

The governing Eqs. (1) and (2), subject to the boundary, initial, and dynamic interface conditions listed above, were solved numerically in the liquid phase. The equations were discretized using MacCormack's method; the moving solid/liquid interface was tracked via the method of Wang [11]. To solve the concentration equation we used 1000 nodes, concentrated near the solid/liquid interface to resolve the concentration gradient. We required only 100 nodes distributed uniformly to solve the energy equation over the same domain. Further refinement of the mesh yielded no further changes in the results, and so the numerical results presented here may be considered mesh-independent.

The physical properties of YSZ [15] used for the simulations are given in Table 2. Results were calculated for a 10 μm thick splat, admittedly thicker than the splat of Fig. 3(b) that is about 3μm thick. It should be noted, however, that our results are characterized by large variations of temperature, concentration, and interface velocity only in the first micron or two of the 10 μm splat, and that the results changed very little when we set the splat thickness to 5 μm. The initial temperature $T_0 = 3250$ K; the nominal yttria concentration $C_0 = 8$ wt.%. At the splat/substrate interface, we prescribed a value of the heat transfer coefficient in the range $h = 5.0 \times 10^5$ to 1.0×10^7 $\mathrm{Wm^{-2}K^{-1}}$, that is usually associated with thermal spray splat solidification. The equilibrium melting temperature of YSZ is 2950 K [15]; we specified an initial undercooling of either 150 or 700 K, leading to the onset of grain growth when the temperature at the splat/substrate interface initially reached 2800 or 2250 K, respectively. The 150 K undercooling was also specified by Wang [11]; the 700 K undercooling comes from Fig. 4, for the grain size we observed experimentally.

Table 2
Physical properties of YSZ used in the calculations [15].

Parameter	Units	YSZ
T_m	K	2950
D_L	$\mathrm{m^2\ s^{-1}}$	1.0×10^{-9}
D_s	$\mathrm{m^2\ s^{-1}}$	$\sim 10^{-15}$
k_e		2.1
κ_L	$\mathrm{Wm^{-1}\ K^{-1}}$	3
κ_S	$\mathrm{Wm^{-1}\ K^{-1}}$	2
C_{PL}	$\mathrm{J\ kg^{-1}K^{-1}}$	713
C_{PS}	$\mathrm{J\ kg^{-1}K^{-1}}$	580
ρ_L	$\mathrm{kg\ m^{-3}}$	5890
ρ_S	$\mathrm{kg\ m^{-3}}$	5890
m_e	$\mathrm{K\ wt.\%^{-1}}$	2.9
Q	$\mathrm{J\ kg^{-1}}$	8.12×10^5
V_D	$\mathrm{ms^{-1}}$	1
μ	$\mathrm{ms^{-1}\ K^{-1}}$	0.0012

Although we assume that the liquid nucleates directly to the tetragonal phase during rapid solidification, we used the value of the equilibrium liquidus slope $m_e = 2.9$ that corresponds to the liquid to cubic transformation from the YSZ phase diagram (Fig. 1), for lack of other data. We specified a Gibbs–Thomson coefficient $\Gamma = 1.0 \times 10^{-9}$ km; we discuss the choice of this value later on. Finally, we set the kinetic coefficient $\mu = 0.0012\ \mathrm{ms^{-1}K^{-1}}$ [11], and the relaxation time $\tau_D = \frac{D}{V_D^2} = 1.0 \times 10^{-9}$ s.

4.1. Splat solidification onto a stainless steel substrate

Profiles of T_i and V_i are presented in Figs. 6 and 7, respectively, for four values of h and two values of the undercooling. The profiles depend largely on the magnitude of the heat transfer coefficient h, whether relatively high ($h = 1.0 \times 10^7$ and $5.0 \times 10^6\ \mathrm{Wm^{-2}K^{-1}}$) or low ($h = 1.0 \times 10^6$ and $5.0 \times 10^5\ \mathrm{Wm^{-2}\ K^{-1}}$) [17].

Both T_i and V_i vary most strongly at the onset of solidification, and differences between results as a function of h are then most pronounced. When h is high, the results vary little with undercooling, because regardless of its value, T_i drops very rapidly from the initial liquid temperature

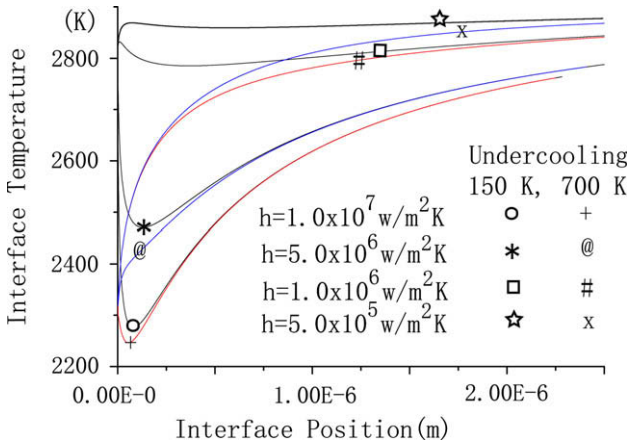

Fig. 6. Interface temperature vs. interface position.

(3250 K) to 2250–2300 K when $h = 1.0 \times 10^7$ Wm^{-2} K^{-1}, and 2250–2450 K when $h = 5.0 \times 10^6$ Wm^{-2} K^{-1}. At the same time V_i increases sharply, from 0.1 ms^{-1} to a maximum of about 0.8 ms^{-1} when $h = 1.0 \times 10^7$ Wm^{-2} K^{-1}, and to 0.6–0.7 ms^{-1} when $h = 5.0 \times 10^5$ Wm^{-2} K^{-1}. The rapid drop in T_i only slows when solidification begins; as the interface accelerates, a strong latent heat release begins, that compensates for the large heat flux to the substrate and allows the interface temperature and velocity to stabilize.

On the other hand, when heat transfer to the substrate is relatively low, the initial T_i and V_i profiles do not vary as dramatically, and are much stronger functions of undercooling than h. When the undercooling is only 150 K, the underside of the splat quickly reaches this temperature despite the small value of h, but the interface velocity only increases to slightly more than 0.1 ms^{-1}, and the interface temperature reaches a minimum value of only 2800 K. On the other hand, when the undercooling is 700 K and yet the heat transfer is relatively low, it takes longer for the underside of the splat to reach the undercooling temperature, and so the interface accelerates much more when solidification begins. The strong latent heat release then acts very quickly to slow the interface (because h is lower), and so both T_i and V_i approach equilibrium values much more quickly than if h were higher.

Fig. 8 presents C_S vs. position of the solidification front (plotted on a log scale). Very early on, because the liquidus slope of YSZ is positive (Fig. 1), the partition coefficient is greater than one and so $C_S > C_0$ for all results. Early values of C_S depend largely on the undercooling: at 150 K, solidification begins more quickly, interface velocities are relatively lower, and so solute segration is higher, than when the undercooling is 700 K. As well, for either value of undercooling, segregation is higher when h is lower, again because V_i is lower. Also note that the relative difference between C_S profiles when undercooled 150 and 700 K is larger than the corresponding profiles of T_i and V_i in Figs. 6 and 7, respectively, because according to Eq. (8), C_L is related to T_i and V_i by the coefficients μ^{-1} and m, which are both greater than one, and $C_S = k_f C_L$. Finally, note that all of the curves show that C_S approaches C_0 (8 wt.%) at steady state, which confirms mass conservation.

Figs. 9 and 10 illustrate the liquid side temperature and concentration gradients vs. position of the solidification

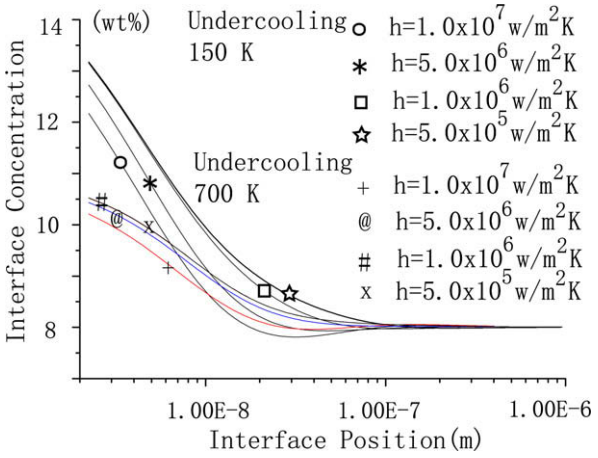

Fig. 8. Interface concentration on solid side vs. interface position.

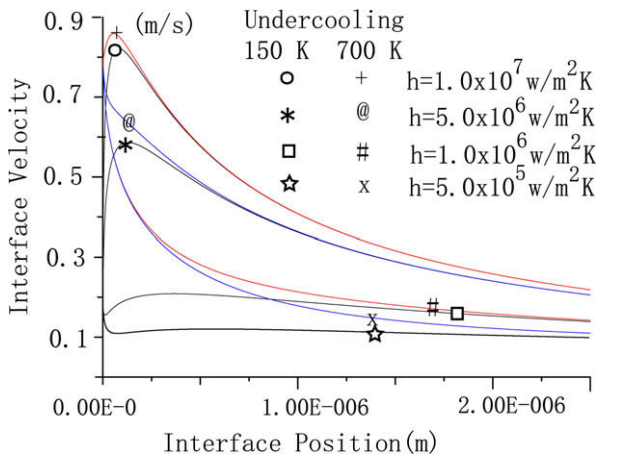

Fig. 7. Interface velocity vs. interface position.

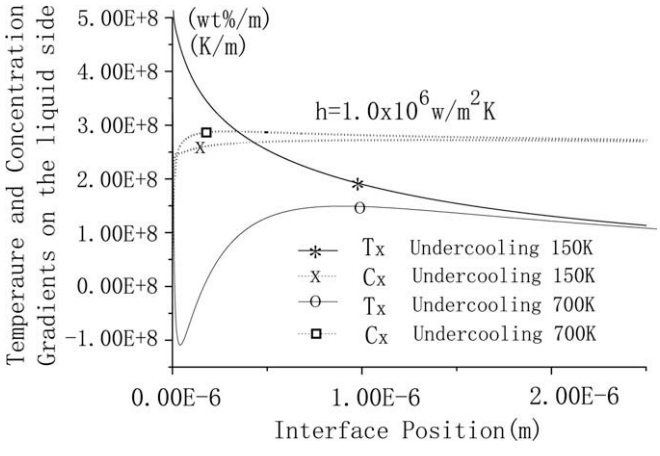

Fig. 9. Temperature and concentration gradients vs. interface position, for $h = 1.0 \times 10^6 Wm^{-2}K^{-1}$.

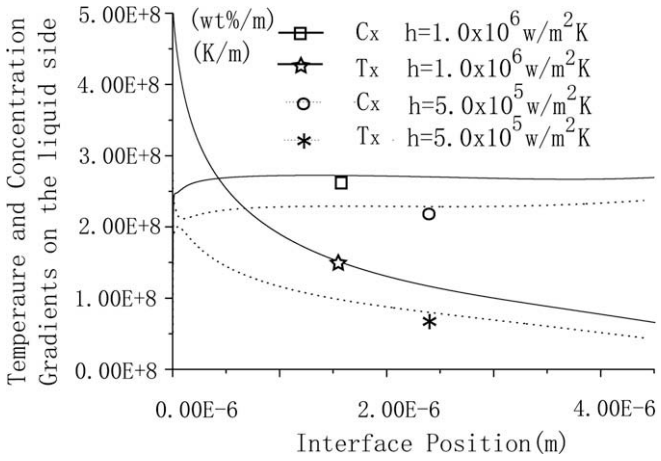

Fig. 10. Temperature and concentration gradients vs. interface position, for 150 K undercooling.

front: Fig. 9 for $h = 1.0 \times 10^6$ Wm^{-2} K^{-1} at the two different undercoolings, Fig. 10 for 150 K undercooling at two different values of h. From Fig. 9, the concentration gradient profiles are largely independent of undercooling; the profiles increase slightly early on, before reaching a stable value. Fig. 10 illustrates that the magnitude of the concentration gradients is proportional to h. The temperature gradients, on the other hand, vary dramatically with undercooling. When undercooling is 150 K, the gradient decreases gradually from a high value. When the undercooling is 700 K, the temperature gradient drops dramatically, reaches a minimum, and then recovers, and gradually approaches the value of the gradient at 150 K. The variation of the temperature gradient with h is less dramatic; as with concentration, the gradient scales with h.

Fig. 11 illustrates predictions of planar-to-cellular interface transformations. It turns out that the model only predicted such transformations within a subset of the parameter space that we explored. Specifically, we varied $5.0 \times 10^5 \leq h \leq 1.0 \times 10^7$ Wm^{-2} K^{-1} and $1.0 \times 10^{-9} \leq \Gamma \leq 1.0 \times 10^{-7}$ mK, but only observed transformations at low values of h and $\Gamma = 1.0 \times 10^{-9}$ mK, which is smaller than typical values usually assigned to Γ [11]. Referring to Fig. 11, one can see that the transformations are largely functions of h. With $h = 1.0 \times 10^6$ Wm^{-2} K^{-1}, the transformation occurs when the solidified layer is around 3.2 μm thick; when $h = 5.0 \times 10^5$ Wm^{-2} K^{-1} the transformation occurs more quickly, at 1.7 μm. In both cases the initial tip radius is around 20 ~ 25 nm, although the stable range at the lower value of h is relatively larger. With $h = 1.0 \times 10^6$ Wm^{-2} K^{-1}, the results appear not to be a function of undercooling at all. With $h = 5.0 \times 10^5$ Wm^{-2} K^{-1}, small differences can be observed: when the undercooling is 700 K, there is a planar-to-cellular interface transition at the very first moment of solidification, and then another transition occurs that reverts the cellular interface back to a planar interface at about 0.1 μm; the planar to cellular transition then occurs again, slightly earlier than when the undercooling is 150 K.

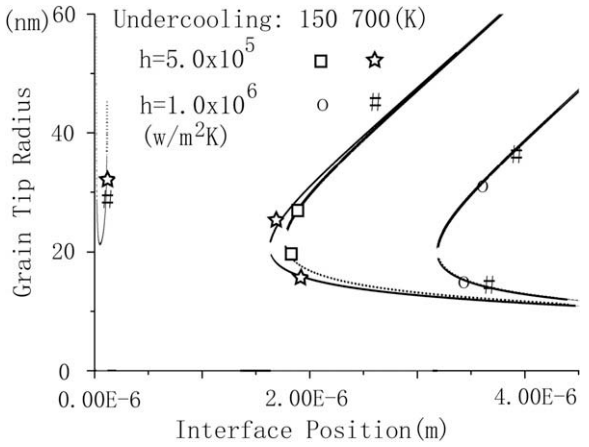

Fig. 11. Grain tip radius vs. interface position, with $\Gamma = 1.0 \times 10^{-9}$ mK.

How to determine primary cellular spacing is still being studied [21]. According to Lu et al. [22], the primary cellular spacing will be about twice the tip radius. Based on this assumption, the results of Fig. 11 suggest an average initial cellular spacing of about 40 ~ 50 nm. Most experimental results yield similar values for thermal sprayed coatings (Fig. 3). However, keep in mind that we assumed a very low value of Γ in order to predict the transformation. More realistically, the above results suggest that there is no transformation, which implies that the size of the columnar grains ought to be determined from nucleation theory (Eq. (13)).

4.2. Splat solidification onto a previously deposited splat

So far we have presented results of a single splat landing on a stainless steel substrate. In practice, most splats build on previously deposited ones, which are either solid or still liquid. To simulate multiple splat deposition, we assumed surface temperatures in the range 573–1073 K, and a lower heat transfer coefficient $h = 5.0 \times 10^5$ Wm^{-2} K^{-1}, an estimate based on knowing the splat thickness, heat conduction properties of YSZ, and the thermal contact resistance between splats. Temperature gradients are pre-

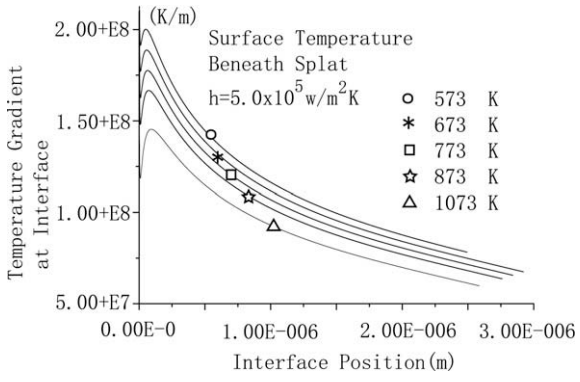

Fig. 12. Temperature gradient vs. interface position, for rapid solidification of a splat onto a previously deposited one.

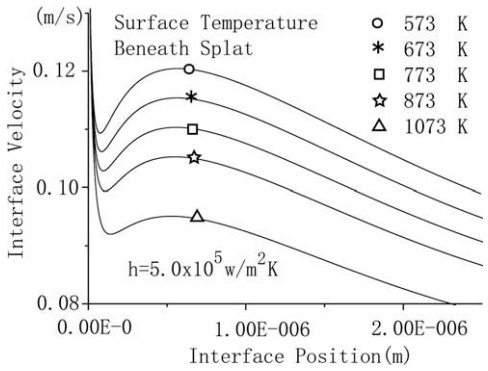

Fig. 13. Interface velocity vs. interface position, for rapid solidification of a splat onto a previously deposited one.

sented in Fig. 12. As the surface temperature beneath the splat increases from 573 to 1073 K, the temperature gradient decreases. The results reveal that the temperature gradient for YSZ is relatively smaller for these cases than when impacting onto a stainless steel substrate, due to the lower heat conductivity of YSZ. Finally, we saw no interface transformation in this set of simulations.

Fig. 13 illustrates that V_i decreases as the temperature beneath the splat increases. The differences between the V_i profiles are almost linearly related to the temperature of the previously deposited splat. Compared to Fig. 6, V_i for multiple splat deposition is much smaller, and so less non-equilibrium behavior is expected.

5. Conclusions

This paper examines the heat and mass transfer behavior of a thermal spray YSZ splat in the very short time after impact onto a substrate, including an analysis of the key parameters that control the solidification behavior and yttria distribution within the splat. Coupled to a one-dimensional interface tracking method, the model effectively simulates non-equilibrium phase change of a binary system. The heat transfer coefficient is assumed relatively low, based on experimental observation of oxide layers existing at the surface of splats; this dramatically influences the solidification front velocity. The interface velocity and the interface concentration and temperature gradients are the main parameters that define the interface morphology.

The paper also presents corresponding experimental results that show columnar grains in a splat cross-section. Microstructure predicted from simulation is very close to that obtained experimentally, when $h = 1.0 \times 10^6$ Wm^{-2} K^{-1}. Interface transformation from planar to cellular occurs when the temperature gradient is low. As the cooling rate increases, the planar interface is the dominant morphology of the solidification front. The calculated primary cellular spacing, which is used to define the grain size is very similar to experimental results.

Finally, droplets also impact onto previously deposited splats. Simulation results indicate relatively lower interface velocities and no interface transformation, because of the high-temperature gradient.

References

[1] Wilkins CR, Wallace FJ, Zajchowski PH. In: 8th International Thermal Spraying Conference 1979:10 Am Welding Soc; 1979.
[2] Ji Z, Haynes JA, Ferber MK, Rigsbee JM. Surf Coat Technol 2001;135:109.
[3] Heiman RB. Plasma spray coating: principles and applications. Weinheim: Wiley-VCH; 1996.
[4] Salimijazi HR, Pershin L, Coyle TW, Mostaghimi J, Chandra S, Lau YC, Rosenzweig L, Moran E. J Therm Spray Technol 2007;16:291.
[5] Chraska T, King AH. Thin Solid Films 2001;397:30.
[6] McDonald A, Lamontagne MM, Chandra S, Moreau C. International Thermal Spray Conference; 2006.
[7] Sampath S, Jiang XY, Matejicek J, Leger AC, Vardelle A. Mater Sci Technol Ser 1999;A272:181.
[8] Salimijazi HR, Pershin L, Coyle TW, Mostaghimi J, Chandra S, Lau YC, Rosenzweig L, Moran E. J Therm Spray Technol 2007;16:580.
[9] Chandra S, Fauchais P. J Therm Spray Techn 2009;18:148.
[10] Wang G-X, Prasad V, Sampath S. Metall Mater Trans A 2000;31:735.
[11] Wang G-X, Goswami R, Sampath S, Prasad V. Mater Manuf Process 2004;19:259.
[12] Robert C, Vardelle A, Gobin D, Fauchais P. High Temp Mater P 1998;2:225.
[13] Lahmar-Mebdoua Y, Vardelle A, Fauchais P, Gobin D. High Temp Mater P 2007;11:191.
[14] Cantor B, Kim WT, Bewlay BP, Gillen AG. J Mater Sci 1991;26:1266.
[15] Liu H, Bussmann M, Mostaghimi J. J Therm Spray Technol 2009;52:1177.
[16] Sobolev SL. Phys Rev E 1997;55:6845.
[17] McDonald A, Moreau C, Chandra S. Intl J Heat Mass Tran 2007;50:1737.
[18] Herlach DM, Holland-Moritz D, Galenko PK. Metastable solids from undercooled melts. Oxford: Pergamon Press; 2007.
[19] Sampath S, Herman H. J Therm Spray Technol 1996;5:445.
[20] Trivedi R. Mater Sci Eng A 1994;178:129.
[21] Kurz W, Fisher DJ. Fundamentals of solidification. Zurich: Trans Tech 1992.
[22] Lu S, Hunt JD, Kurz W. Acta Metall Mater 1994;42:1653.